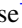# Simulations of sphere-forming diblock copolymer melts

Anshul Chawla ⓘ, Frank S. Bates ⓘ, Kevin D. Dorfman ⓘ,* and David C. Morse†

Department of Chemical Engineering and Materials Science, University of Minnesota–Twin Cities,
421 Washington Ave. SE, Minneapolis, Minnesota 55455, USA

Molecular dynamics simulations are used to study melts of asymmetric sphere-forming diblock copolymers with two significantly different values of the invariant degree of polymerization, $\overline{N} = 3820$ and 960. In both systems, changes in parameters that correspond to decreasing temperature lead to the appearance of micelles at a critical micelle temperature (CMT) and crystallization at a lower order-disorder transition temperature (ODT). The CMT is identifiable in simulations by the appearance of large clusters with a strongly segregated core region, but has no equally clear signature in scattering experiments on systems of modest $\overline{N}$. The value of the product χN at the CMT (where χ is the Flory-Huggins parameter and N is degree of polymerization) is close to that predicted by SCFT for the ODT, while the value at the actual ODT is larger and increases with decreasing $\overline{N}$. Micelles exhibit significant and comparable dispersity in aggregation number in the crystalline and liquid phases near the ODT. Both the liquid and crystal phases exhibit transient dimers consisting of pairs of neighboring spherical micelles with cores connected by a bridge of core-block material.

I. INTRODUCTION

Melts of highly asymmetric AB diblock copolymers tend to self-assemble into spherical micelles with a core containing the minority block. A variety of experiments and simulations [1–8] suggest the existence of three temperature regimes in systems with a positive heat of mixing (the usual case): The high-temperature regime produces a molecularly disordered state with relatively small composition fluctuations. With decreasing temperature, micelles appear over a relatively narrow range of temperatures near a critical micelle temperature (CMT), forming a liquid of micelles over an intermediate temperature range. Upon further decreasing temperature, this liquid crystallizes at an order-disorder transition temperature (ODT), creating an ordered phase. The most commonly observed crystalline arrangement of micelles is a body-centered cubic (BCC) lattice, but a variety of more complicated Frank-Kasper and quasicrystalline arrangements have been observed [9–19].

Three different types of experiments have provided evidence for the existence of a liquid of micelles over a range of temperatures above the ODT. First, several early transmission electron microscopy (TEM) images showed a dense, disordered arrangement of spherical micelles at temperatures above the ODT [6,7]. Second, results of small angle x-ray and neutron scattering (SAXS and SANS) experiments in the liquid phase near the ODT show the presence of a secondary peak or shoulder in plots of scattering intensity $I(q)$ versus scattering wavenumber q, consistent with the picture of a disordered micellar phase [1–5]. An early analysis by Kinning

and Thomas [1] showed that the existence and approximate position of this secondary feature could be explained by a model of the melt as a strong correlated liquid of spherical micelles, using the Percus-Yevick theory of hard spheres [20] to model a structure function factor that describes correlations in micelle center-of-mass positions. This analysis was repeated and refined in several subsequent scattering studies [2–5]. Finally, measurements of linear viscoelastic properties have also shown the existence of an elastic-like response at high frequencies that is believed to be the result of stress created by straining a disordered micro-phase separated state [21].

Establishing the theoretical basis for the disordered micelle regime has been a longstanding challenge. To establish notation, consider an incompressible melt of AB diblock polymers with degree of polymerization N, volume fraction f for the minority block, Flory-Huggins parameter χ, statistical segment lengths b_A and b_B for A and B monomers, respectively, and a total monomer concentration $c = 1/v$, where v is a monomer reference volume. Let g denote the free energy per polymer divided by $k_B T$, where k_B is Boltzmann's constant and T is absolute temperature. Self-consistent field theory (SCFT), the most widely used theory for describing block polymer phase behavior, yields a prediction for g in a given phase that depends only on the dimensionless parameters χN, f, and b_A/b_B, which we refer to as the SCFT state parameters. We focus hereafter on conformationally symmetric systems with $b_A = b_B = b$, for which the remaining state parameters are χN and f. SCFT predictions for structural lengths such as the micelle core radius and equilibrium unit-cell dimensions in a crystalline phase of such a system are given by R times a dimensionless function of the same state parameters, where $R = b\sqrt{N}$ is the end-to-end distance of the polymer. SCFT predicts the simultaneous appearance and crystalliza-

*dorfman@umn.edu
†morse012@umn.edu

tion of micelles at a first-order transition from a micelle-free disordered phase to a crystal of micelles. This predicted order-disorder transition occurs at a critical value of χN, denoted here by $(\chi N)_{\text{odt}}^{\text{scf}}$, that depends only on f. The systems simulated here all have $f = 0.125$ for which $(\chi N)_{\text{odt}}^{\text{scf}} = 36.6$ [22].

The magnitude and nature of deviations from SCFT predictions for block copolymer melts are controlled by the invariant degree of polymerization $\overline{N} = N(cb^3)^2$. The parameter $\overline{N}^{1/2}$ is proportional to the ratio R^3/Nv of the volume R^3 pervaded by a random walk polymer to the occupied volume per chain Nv. Theoretical analyses [23–25] and simulations of simple models [26–32] both suggest that SCFT becomes exact in the limit $\overline{N} \to \infty$, and that deviations from SCFT exhibit a universal dependence on $\overline{N}$, independent of many details of a particular simulation model or experimental system. Specifically, simulations of symmetric and modestly asymmetric diblock copolymers have provided strong evidence for the hypothesis that g is a nearly universal function of $\overline{N}$ and the SCFT state parameters [29,30,32]. However, SCFT is based on a qualitatively incorrect picture of the disordered phase near the ODT because it assumes random mixing at a monomer level within the disordered phase. In systems with experimentally relevant values of $\overline{N}$, the disordered phase of a diblock copolymer melt near the ODT is instead found to contain disordered but rather strongly segregated A and B domains [29,30,33]. Highly asymmetric copolymers with $f < 0.2$ such as those simulated here, form disordered arrangements of spherical micelles [1–7]. The appearance of local segregation without crystalline order stabilizes the disordered phase, and pushes the value of χN at the actual order-disorder transition $(\chi N)_{\text{odt}}$ to values significantly greater than $(\chi N)_{\text{odt}}^{\text{scf}}$.

There are two key prior theoretical studies of the disordered micelle regime that are relevant to the present paper. In the first, Dormidontova and Lodge presented a relatively simple and qualitatively correct theory of thermodynamics in sphere-forming diblock copolymers that predicts the existence of a micellar liquid regime at intermediate temperatures [34]. This theory extended earlier work by Semenov [35,36] on a strong-stretching theory for asymmetric copolymers, which provided analytic expressions for both the free energy of an isolated micelle and for an effective interaction between pairs of micelles. Dormidontova and Lodge [34] combined this with a simple treatment of the effects of micelle and unimer translational entropy, and allowed for the possible formation of a disordered micellar fluid. The resulting theory yields predictions for both an apparent CMT and the ODT. In the second relevant study, Wang *et al.* presented an analysis of the appearance of micelles within the disordered phase that is based upon a numerical SCFT calculation of the free energy of formation of an isolated micelle within an otherwise disordered melt [33]. This formation free energy, denoted here by W_m, becomes negative at values of χN greater than a critical value, denoted here by $(\chi N)_{\text{m}}^{\text{scf}}$, thus favoring the proliferation of micelles for $\chi N > (\chi N)_{\text{m}}^{\text{scf}}$. The value of $(\chi N)_{\text{m}}^{\text{scf}}$ was found to be very similar but slightly greater than the value $(\chi N)_{\text{odt}}^{\text{scf}}$ at which SCFT predicts formation of a crystal to become favorable. The slight difference reflects the fact that the crystal phase is stabilized by the existence of weak attractions between

neighboring micelles in a crystal. For example, for the case $f = 0.1$ that they studied in greatest detail, Wang *et al.* found $(\chi N)_{\text{m}}^{\text{scf}} = 48.14$, while we obtain $(\chi N)_{\text{odt}}^{\text{scf}} = 47.95$ for a BCC crystal candidate phase. The difference $(\chi N)_{\text{m}}^{\text{scf}} - (\chi N)_{\text{odt}}^{\text{scf}}$ is, however, much smaller than other differences of interest here, such as the difference $(\chi N)_{\text{odt}} - (\chi N)_{\text{odt}}^{\text{scf}}$, and so is negligible for our current purposes.

In the present contribution, we report data for coarse-grained bead-spring diblock copolymer melt simulations performed for two models with significantly different values of $\overline{N}$. We recently provided a preliminary report [8] for a system with $\overline{N} = 3820$, focusing on the development of methods to identify the CMT. Here, we present a more thorough analysis of those data [8] and new data for a system with $\overline{N} = 960$, with the latter system bringing to the fore the impact of fluctuation effects that should be prominent for experimentally-relevant degrees of polymerization. Where appropriate, we reproduce some results reported in Ref. [8] alongside new data for $\overline{N} = 960$ so that the impact of lowering $\overline{N}$ is readily discernible. The analysis presented here involves a detailed structural characterization, comparisons to SCFT predictions, and analyses of both ordered and disordered phases. In addition to the additional data at low $\overline{N}$ and the accompanying discussion that did not appear in Ref. [8], this contribution provides an interpretation of the structure factor in the context of Percus-Yevick theory [20], calculation of the number of free chains, comparison of the most probable aggregation number to an estimate from SCFT, computation of the latent heat at the ODT (see Supplemental Material, SM [37]), and a thorough analysis of dimer formation in both the ordered and disordered state, including an analysis of their dynamics (see SM [37]).

II. SIMULATION DETAILS

In this paper we have used constant pressure, constant temperature molecular dynamics (MD) simulations of coarse-grained bead-spring models of asymmetric AB diblock copolymers. Each chain contains N beads, of which $N_B = fN$ are of monomer type B (the minority species), and the remainder of type A. For all systems studied in this paper, $N = 64$ and $N_B = 8$, giving $f = 1/8$.

We use a potential energy with a harmonic bond potential and a soft nonbonded pair interaction similar to that introduced in dissipative particle dynamics simulations, employing choices of parameters used in several previous simulation studies by our group [29–32]. A repulsive nonbonded potential acts between all bead pairs that are separated by a distance r less than a cutoff distance σ, with a potential of the form $\epsilon_{ij}[1 - (r/\sigma)]^2/2$ between beads of types i and j for $r < \sigma$, with $\epsilon_{AA} = \epsilon_{BB}$. We define a parameter $\alpha \equiv (\epsilon_{AB} - \epsilon_{AA})/k_{\text{B}}T$ that is adjusted to control the driving force for microphase separation. Adjacent beads within each chain interact via a harmonic bond potential of the form $\kappa r^2/2$, where κ is a spring constant. Additional details on the simulation method are provided in the SM [37].

We simulate two systems, each of which is defined by a fixed set of choices for all model parameters except α, and simulate each system over a range of values of α. The

TABLE I. Model parameters and properties for models S1 and S2, in units with $k_B T = \sigma = 1$. The self-interaction parameter ϵ_{AA}, spring stiffness κ, and pressure P have fixed values for each model. The monomer concentration c and statistical segment length b are extrapolated values for infinite homopolymers ($\alpha = 0$ and $N \to \infty$). The quantities z, a, and d are coefficients that appear in Eq. (1) for $\chi(\alpha)$.

Model	ϵ_{AA}	κ	c	P	b	z	a	d
S1	25.0	3.406	3.0	20.249	1.088	0.237	0.138	0.438
S2	25.0	1.135	1.5	4.111	1.727	0.0916	−0.00087	0.00420

two systems studied here correspond to models S1-64 and S2-64 as defined in Ref. [30]. These models have previously [29,30] been shown to yield invariant degrees of polymerization $\overline{N} = 960$ (S1-64) and $\overline{N} = 3820$ (S2-64). For clarity in what follows, we will refer to the different simulation systems by their invariant degrees of polymerization since this is the physically relevant descriptor. Previous papers [29,30] further established a relationship between α and the Flory-Huggins interaction parameter χ for each of these models, which was approximated by the function

$$\chi(\alpha) = \frac{z\alpha + a\alpha^2}{1 + d\alpha} \quad . \tag{1}$$

Table I lists values for the fixed input parameters for the two models studied in this paper, along with values of the coefficients z, a, and d and other properties that were obtained in previous papers [29,30] by analyzing simulations of these models; the reader is referred to Ref. [30] for a detailed explanation of the model parameters.

We have also performed simulations to identify conditions under which an initially disordered melt will spontaneously crystallize or an initially ordered crystal will spontaneously melt in systems that are designed so that the periodic simulation unit cell is, as nearly as possible, commensurate with the preferred crystallographic unit cell. The latter results and a discussion on the latent heat of the transition are provided in SM [37]. The number of polymer molecules, denoted by M, was chosen in most simulations so as to approximately accommodate a $3 \times 3 \times 3$ array of BCC unit cells if the system were to crystallize (see SM [37]).

Much of our analysis relies on the identification of physical clusters of molecules that are candidates for identification as micelles. Two molecules are taken to belong to the same cluster if their minority blocks are in close contact, i.e., if the distance between any intermolecular pair of minority block beads from these molecules is less than 0.8σ. This value was selected based on prior simulations of micelles using these models [38], where aggregation numbers using this cutoff were consistent with those obtained by counting the number of chains in a micelle. Using this criterion, we may assign every molecule in the system to a unique cluster. Figure 1 shows a visualization of a micellar cluster identified by this method, in a format that shows the micelle core and the conformation of one molecule.

III. STRUCTURE FACTOR

The structure factor $S(q)$ is defined here as

$$S(q) = \left\langle \frac{1}{V} |\tilde{\psi}(\mathbf{q})|^2 \right\rangle \quad , \tag{2}$$

where $\tilde{\psi}(\mathbf{q}) = \int d\mathbf{r}\, \psi(\mathbf{r}) e^{i\mathbf{q}\cdot\mathbf{r}}$ is a Fourier amplitude of the composition field $\psi(\mathbf{r}) = [c_A(\mathbf{r}) - c_B(\mathbf{r})]/2$, $c_i(\mathbf{r})$ is the concentration of i monomers, V is total system volume, and $q = |\mathbf{q}|$. Figure 2 compares $S(q)$ data for different values of χN for both $\overline{N} = 960$ and the previous data [8] for $\overline{N} = 3820$. The most obvious feature in this figure is the existence of a maximum in $S(q)$ at a wavenumber denoted by q^*.

To identify any secondary features, we fit the data in Fig. 2 to a functional form $S(q) = K S_{\text{RPA}}(q)$, where $S_{\text{RPA}}(q)$, the solid lines in Fig. 2, are the prediction of the random-phase approximation (RPA) [39]. In this fit, the prefactor K and the parameters R_g and χ that are required as inputs to the RPA prediction have all been treated as adjustable parameters that are chosen to fit the data in the vicinity of the peak. The RPA functional fits the data for both models at the lowest value of χN, which in both cases is near $(\chi N)_{\text{odt}}^{\text{scf}} = 36.6$, but the RPA does not fit the results for higher values of χN for neither value of $\overline{N}$. Comparison of the data to this fit helps emphasize the appearance at higher values of χN of a weak shoulder centered around $q R_{g0} \sim 3$–4, where $R_{g0} = b\sqrt{N/6}$ is the unperturbed radius of gyration, which becomes more prominent with increasing χN. The existence of this secondary feature in $S(q)$ was first noted in experimental scattering data by Kinning and Thomas [1], who attributed it to the presence of strong correlations in the positions of micelles within a dense micellar liquid. This secondary shoulder develops at
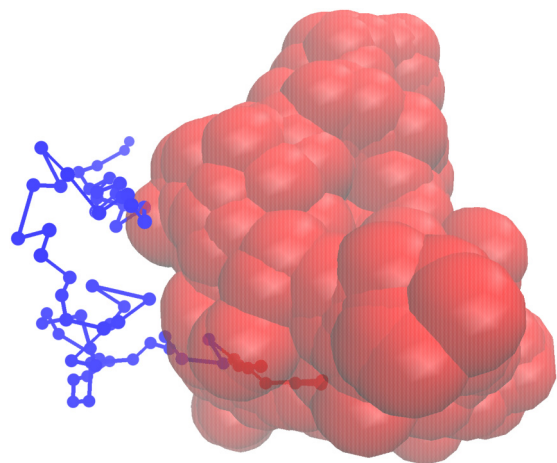

FIG. 1. Visualization of the core of a micellar cluster composed of 83 chains. Minority block beads belonging to all molecules in the cluster are shown as as overlapping translucent red spheres. The conformation of one representative molecule is shown as sequence of points representing beads connected by line segments, with blue points for majority/corona block beads and red points for minority/core block beads.
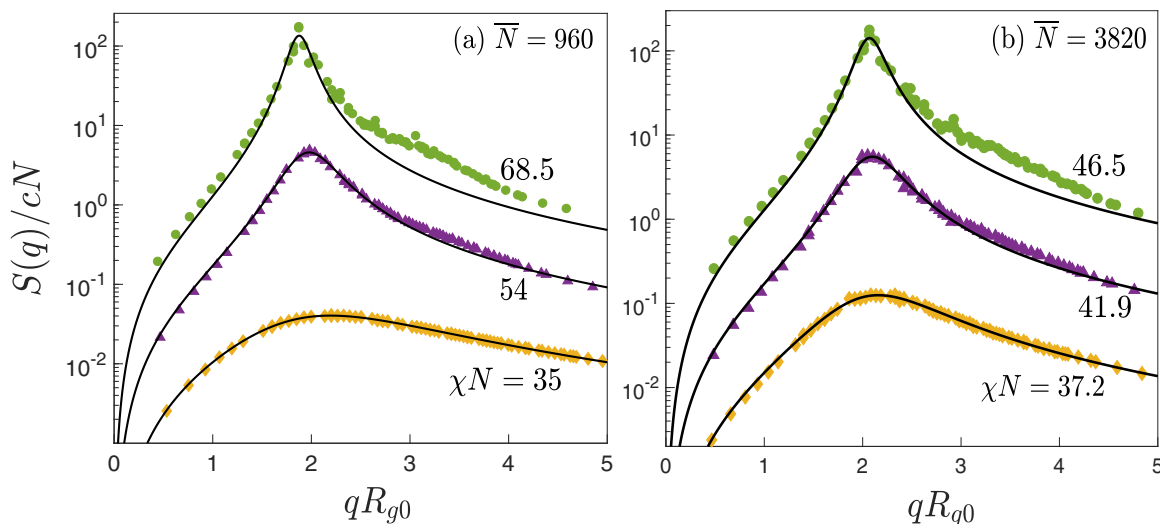
FIG. 2. Structure factor $S(q)$ vs nondimensionalized wavenumber qR_{g0}, for (a) $\overline{N} = 960$ and (b) $\overline{N} = 3820$ at several values of χN. $R_{g0} = b\sqrt{N/6}$ is the unperturbed polymer radius of gyration. Solid lines are fits of behavior near the peak to the functional form predicted by the random-phase approximation (RPA). Panel (b) reproduced with permission from Ref. [8].

significantly lower values of χN in the system with larger value of $\overline{N}$; note that the strength of the shoulder in the system with $\overline{N} = 3820$ and $\chi N = 46.5$ [Fig. 2(b)] is greater than that seen in the system $\overline{N} = 960$ [Fig. 2(a)] at a higher value of $\chi N = 54$, and comparable to that observed for $\overline{N} = 960$ at the much higher value of $\chi N = 68.5$.

To discern the deviations between the RPA model and the simulation data across the full range of χN, Fig. 3 shows how the normalized inverse peak intensity $cNS^{-1}(q^*)/2$ within the disordered phase changes with χN for both invariant degrees of polymerization. The results for $\overline{N} = 3820$ have been reported previously [8]. A strongly first-order ODT of the type predicted by SCFT would be accompanied by a dramatic increase in $S(q^*)$, and a corresponding decrease in $S^{-1}(q^*)$, due to the appearance of Bragg peaks in $S(q)$. Appearance
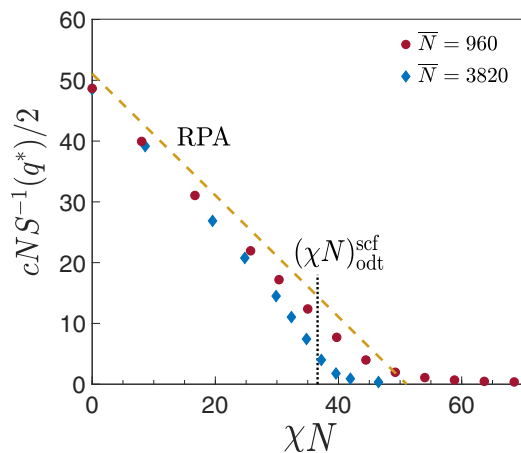
and proliferation of disordered micelles within a sufficiently narrow range of values of χN near $(\chi N)_{\mathrm{odt}}^{\mathrm{scf}}$ also would be expected to produce a sudden increase in $S(q^*)$, or, equivalently, a sudden decrease in $S^{-1}(q^*)$, with increasing χN, due to the appearance of additional scattering from micelles. A hint of this type of behavior is visible in Fig. 3 for $\overline{N} = 3820$, which exhibits an inflection at a value of χN near $(\chi N)_{\mathrm{odt}}^{\mathrm{scf}}$ at which the magnitude of the slope $dS^{-1}(q^*)/d(\chi N)$ appears to show a weak maximum. There is, however, no sign of such an inflection in corresponding results for $\overline{N} = 960$. Rather,
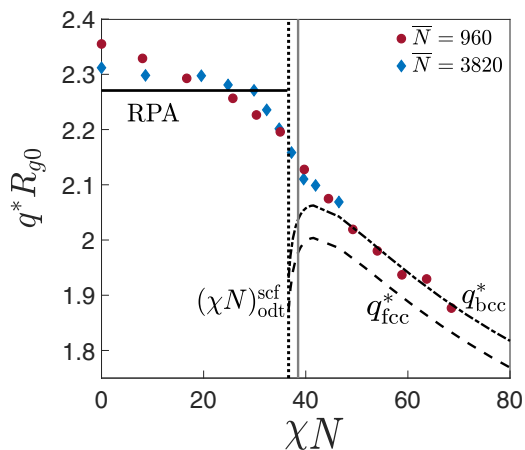

FIG. 3. Nondimensionalized inverse peak intensity $cNS^{-1}(q^*)/2$ vs χN for $\overline{N} = 960$ (solid-red circles) and $\overline{N} = 3820$ (solid-blue diamonds). The diagonal dashed line is the RPA prediction. The vertical-dotted line marks location of $(\chi N)_{\mathrm{odt}}^{\mathrm{scf}}$. Error bars are smaller than the data points and provided in the SM [37].

FIG. 4. Normalized peak wavenumber q^*R_{g0} vs χN for $\overline{N} = 960$ (solid circles) and $\overline{N} = 3820$ (solid-blue diamonds), where $R_{g0} = b\sqrt{N/6}$. The dotted-vertical line and the solid-vertical-gray line marks the disordered-FCC phase transition at $(\chi N)_{\mathrm{odt}}^{\mathrm{scf}} = 36.6$ and the order-order transition from FCC to BCC at $\chi N = 38.5$, respectively. The solid-horizontal-black line shows the RPA prediction for q^*R_{g0} in the disordered phase, which is shown only for $\chi N < (\chi N)_{\mathrm{odt}}^{\mathrm{scf}}$. The dot-dashed and dashed curves plotted for $\chi N > (\chi N)_{\mathrm{odt}}^{\mathrm{scf}}$ show SCFT predictions for the value of q^*R_{g0} corresponding to the primary Bragg peaks in the BCC and FCC phases, respectively.
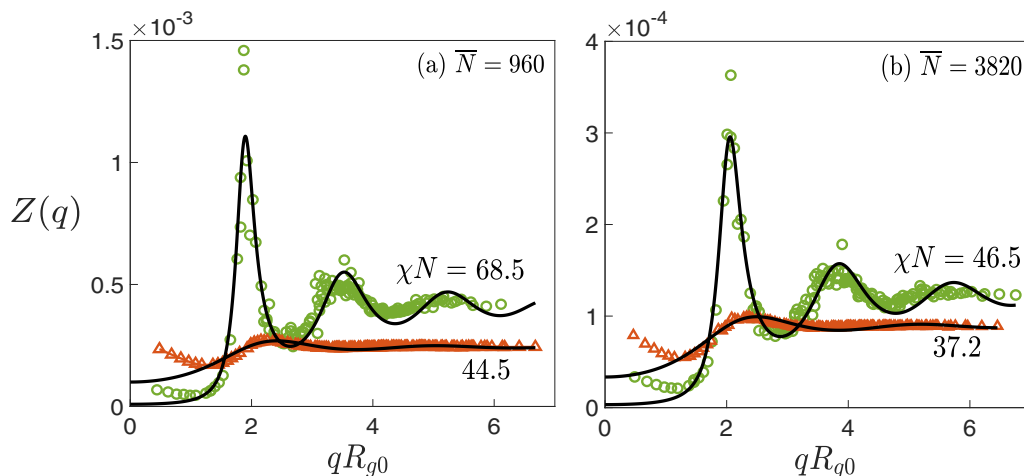
FIG. 5. Symbols show the calculated intermicellar correlations $Z(q)$ at two values of χN for (a) $\overline{N} = 960$ and (b) $\overline{N} = 3820$. The solid lines in the plot are fits to the Percus-Yevick theory, in which the sphere radius R_{hs}, and the effective volume fraction, η, and an overall constant of proportionality are adjusted to fit the data. The resulting fit parameters are in Table II. Note that a different ordinate scale is used for each $\overline{N}$.

$S^{-1}(q^*)$ versus χN exhibits a uniformly positive curvature and flattening out near an apparent spinodal value analogous to that seen in corresponding plots of results for more symmetric copolymers [26,28,40]. This difference in the behavior of the peak intensity in systems with different values of $\overline{N}$ suggests that micelles proliferate over a smaller range of values of χN in systems with larger values of $\overline{N}$.

The location of the structure factor peak at q^* provides further information on the intermicellar distance. Figure 4 thus compares simulation results for both invariant degrees of polymerization to (i) RPA predictions for q^* for $\chi N < (\chi N)^{\text{scf}}_{\text{odt}}$ and (ii) SCFT predictions for the wavenumber of the primary family of Bragg peaks for $\chi N > (\chi N)^{\text{scf}}_{\text{odt}}$, where q^* is made dimensionless with R_{g0}. The results for $\overline{N} = 3820$ have been reported previously [8]. Data for both values of $\overline{N}$ exhibit a monotonic decrease of q^* with increasing χN. Values of q^* at $\chi N = 0$ are slightly greater than those predicted by the RPA for both models, with closer agreement between the RPA prediction for $\chi N < (\chi N)^{\text{scf}}_{\text{odt}}$ and the larger $\overline{N}$. For $\chi N > (\chi N)^{\text{scf}}_{\text{odt}}$, simulation results for q^* in the disordered phase seem to approach the SCFT predictions for the BCC phase that SCFT predicts to be stable over most of this range. This behavior of q^* is broadly analogous to that seen in previous simulations of the disordered phase of less asymmetric copolymers [28,31].

The structure factor $S(q)$ measured here is analogous to the scattering intensity $I(q)$ measured in small-angle x-ray and neutron scattering studies. In an analysis that was introduced by Kinning and Thomas [1] and refined in subsequent papers [2,3,5,7], $I(q)$ in the disordered phase of asymmetric copolymers was modeled as scattering from a liquid of spherical micelles. In those analyses, experimental data for $I(q)$ are compared to a model in which $S(q)$ is expressed as a product of a form factor for a spherical micelle core times a structure factor for the centers of the micelle cores, denoted here by $Z(q)$. The Percus-Yevick (PY) theory for hard spheres [20] is used to model the micelle structure factor $Z(q)$, while treating the sphere radius and effective volume fraction as adjustable parameters. The resulting model was shown [1–5] to account naturally for the appearance of a primary peak and secondary shoulder in $S(q)$ with approximately the observed ratio of characteristic wavenumbers, in a model in which both features are assumed to be consequences of intermicellar correlations in a dense fluid.

Using our simulation data, we can directly measure the relevant micelle structure function $Z(q)$, and thereby test the assumptions underlying this analysis. Our calculation of $Z(q)$ is based on an analysis of "micellar" clusters, defined as clusters identified using the algorithm described in Sec. II for which the aggregation number lies within a specified range of values. Let x_n denote the fraction of chains that belong to clusters of aggregation number n. In systems that contain well defined micelles, the distribution x_n exhibits a local minimum and a local maximum, as discussed in detail in Sec. IV. To compute $Z(q)$, micellar clusters are taken to be those for which the aggregation number n lies between the value at which x_n exhibits a local minimum and 1.6 times the value at the local maximum. For each such micellar cluster, we define a central position defined as the center-of-mass of the minority block beads of molecules that belong to the cluster (i.e., the center of mass of the core). The micelle structure function

TABLE II. Values of R_{hs}/Rg_0, and η extracted from the fits of the intermicellar correlation $Z(q)$ to the Percus-Yevick theory [20]. The data were fit to a prediction of the form $Z(q) = KZ_{PY}(qR_{hs}, \eta)$, where $Z_{PY}(qR_{hs}, \eta)$ denotes the Percus-Yevick prediction of the structure factor of hard spheres of diameter R_{hs} and volume fraction η. The parameters K, R_{hs}, and η are adjusted to fit the data.

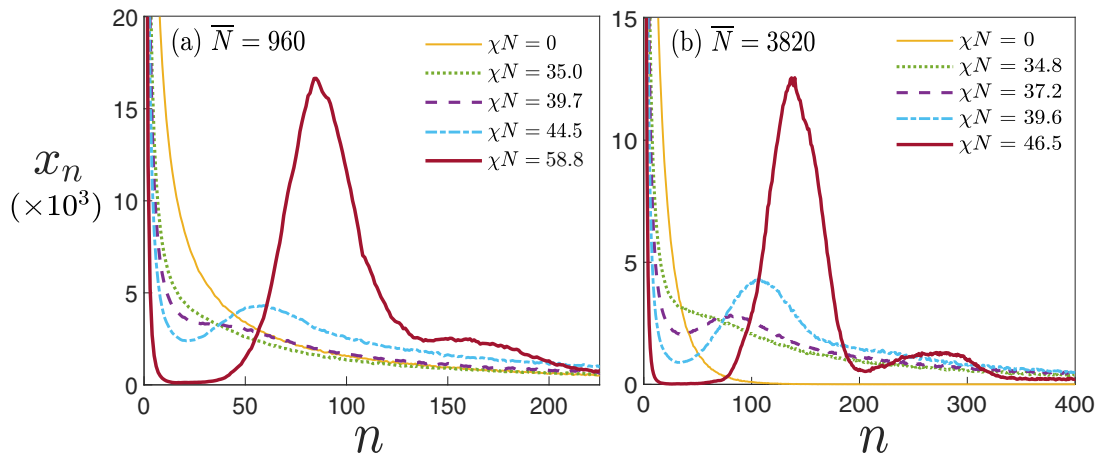| $\overline{N}$	α	χN	R_{hs}/Rg_0	η
960	2.5	44.5	1.228	0.1132
960	3.75	68.5	1.8098	0.4648
3820	7	37.2	1.1917	0.12414
3820	9	46.5	1.6503	0.44237

FIG. 6. Mole fraction x_n of chains that belong to clusters of aggregation number n for (a) $\overline{N} = 960$ and (b) $\overline{N} = 3820$. Note that the axis limits differ between panels. Panel (b) reproduced with permission from Ref. [8].

$Z(q)$ is then defined by the sum

$$Z(q) = \sum_{j,k} \left\langle \frac{1}{V} e^{i\mathbf{q}\cdot(\mathbf{R}_j - \mathbf{R}_k)} \right\rangle \quad, \tag{3}$$

where $\mathbf{R}_j$ represents the central position of micellar cluster number j. The sums over j and k are taken over all micellar clusters.

Figure 5 provides simulation results for $Z(q)$ for two values of χN for each of the two values of $\overline{N}$. For each value of $\overline{N}$, the higher value of χN shown corresponds to a state in which $S(q)$ exhibits both a primary peak and a clear secondary shoulder. The corresponding results for $Z(q)$ exhibit both a primary peak at a value of $qR_{g0} \simeq 2$ close to the value at which $S(q)$ in Fig. 2 exhibits a primary maximum, and a secondary peak at a value of $qR_{g0} \sim 3.6$ to 3.8 similar to that at which $S(q)$ shows a secondary shoulder. This confirms that the secondary shoulder in $S(q)$ is indeed caused by the existence of a corresponding peak in $Z(q)$, reflecting strong correlations in micelle positions, as suggested by previous analyses of scattering data [1–5]. The lower value of χN corresponds to a state relatively close to the CMT in which $S(q)$ exhibits a primary peak but no secondary shoulder. The corresponding results for $Z(q)$ are now nearly structureless, though $S(q)$ still shows the single pronounced peak seen in Fig. 2 for lower values of χN. This indicates that at these lower values of $\chi N \sim (\chi N)_{\mathrm{odt}}^{\mathrm{scf}}$, $S(q)$ probably cannot be correctly described by a model that attributes all scattering as originating from a liquid of spherical micelles.

IV. CLUSTER POPULATION ANALYSIS

In this section, we characterize micelles in the disordered phase by analyzing results of the cluster analysis described in Sec. II. To begin this analysis, Fig. 6 depicts the fraction x_n of chains with aggregation number n for both models over a range of values of χN. At the higher invariant degree of polymerization (data reported previously [8]) x_n is a monotonically decreasing function of n for all values less than $(\chi N)_{\mathrm{odt}}^{\mathrm{scf}} = 36.6$ (measured values $\chi N \leqslant 34.8$) and develops a local maximum for all values greater than $(\chi N)_{\mathrm{odt}}^{\mathrm{scf}}$ (measured

values $\chi N \geqslant 37.2$). This indicates emergence of proper micelles over a narrow range of values of χN near $(\chi N)_{\mathrm{odt}}^{\mathrm{scf}}$ [8]. Corresponding results for $\overline{N} = 960$ in Fig. 6 are qualitatively similar to those at $\overline{N} = 3820$. Here, x_n is still a monotonically decreasing function of n for $\chi N = 39.7$ and exhibits a weak maximum for $\chi N \geqslant 44.5$. The value of χN at the apparent CMT thus does appear to increase somewhat with decreasing $\overline{N}$, though the results for $\overline{N} = 3820$ suggest that the CMT rapidly approaches $(\chi N)_{\mathrm{odt}}^{\mathrm{scf}}$ with increasing $\overline{N}$ for $\overline{N} > 10^3$.

Under conditions for which proper micelles exist, results of the cluster analysis can be used to quantify the fraction of free chains that remain outside of micelles. We apply this analysis only at values of χN for which x_n exhibits a local minimum and local maximum, and classify chains that belong to clusters of aggregation numbers less than the value of n at the local minimum as "free" chains. Let x_{free} denote the total fraction of such chains, given by the sum of values of x_n from 1 to the value at which x_n is minimum.
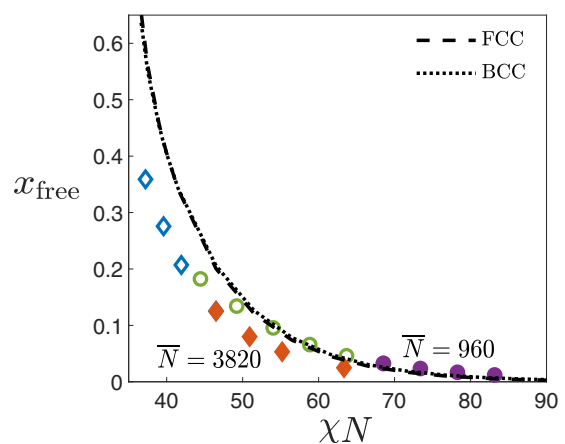

FIG. 7. Fraction of free chains x_{free} as a function of χN from simulations (symbols) and as predicted by SCFT. Diamonds and circles represent simulation results for $\overline{N} = 3820$ and $\overline{N} = 960$, respectively. Open and closed symbols represent results of simulations of disordered and ordered phases, respectively.
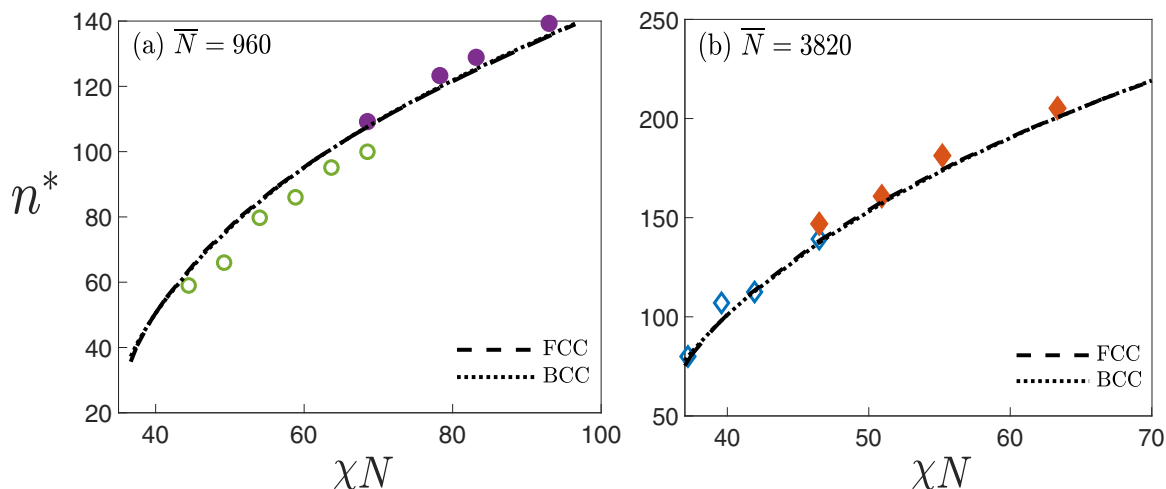
FIG. 8. Most probable micelle aggregation number n^* vs χN for (a) $\overline{N} = 960$ and (b) $\overline{N} = 3820$. Results are shown only for values of χN for which x_n exhibits a local maximum. Open and closed symbols represent results obtained from simulations of disordered and ordered states, respectively. Results obtained from ordered states are shown for all values of χN for which the ordered state remained stable. Lines represent SCFT predictions for BCC and FCC crystals, which are visually indistinguishable on the scale of this plot. Note that the axis limits differ between panels.

Figure 7 shows simulation results for the fraction x_{free} where results from simulations of ordered BCC phases are used throughout the range of values of χN in which the ordered phase is found to remain stable (solid symbols), while results from disordered melts are used at lower values of χN (open symbols). For both values of $\overline{N}$, results from disordered and ordered phases form an apparently continuous line, indicating that crystallization has little if any effect on x_{free}. Moreover, x_{free} is substantial at the lowest value studied ($x_{\text{free}} \simeq 0.2$ to 0.4) and decreases with increasing χN. Figure 7 also compares simulation results to an SCFT prediction of x_{free} that we obtained by measuring the volume fraction of the minority monomer type at the midpoint between two neighboring micelles, and equating this to $f x_{\text{free}}$, with $f = 1/8$. Agreement with this SCFT prediction is reasonably good at larger values of χN, particularly in light of differences between the definitions of x_{free} used in the cluster analysis and the SCFT analysis.

It is also illuminating to examine how the micelle aggregation numbers are influenced by χN and $\overline{N}$. To do so, we define n^* to be the value of n at which x_n is maximum. This quantity is estimated by fitting a region near the peak in x_n to a Gaussian function (using a region within $\pm 20\%$ of the maximum) and approximating n^* by the value of n at the maximum of that Gaussian. Figure 8 shows that n^* increases substantially with increasing χN in both ordered and disordered phases. Results for $\overline{N} = 980$ show a statistically measurable difference in values of n^* from ordered and disordered phases at $\chi N = 68.5$, the lowest value for which the ordered phase was found to remain stable. For $\overline{N} = 3820$, the corresponding difference between values of n^* in the ordered and disordered phases is significantly smaller, and difficult to reliably measure because the difference (if any) is comparable to the scatter in our results for n^*. Results for n^* in the ordered phase are very sensitive to our choice of the number of molecules in the simulation (see SM [37]).

SCFT predictions for n^* in crystalline structures, shown as lines in Fig. 8, were estimated as $n^* = m(1 - x_{\text{free}})$, where m is an SCFT prediction for the total number of molecules per micelle, and x_{free} is the SCFT prediction for the fraction of free chains, computed as described above. The SCFT prediction for m is computed by combining SCFT predictions for the optimal unit cell size with values of the statistical segment length b and monomer concentration c appropriate to the simulation model (Table I). These predictions agree rather well with measurements of n^* in both the disordered and ordered micellar state.

While we have focused on the disordered liquid phase thus far, the cluster analysis may be applied in simulations of ordered micelle crystals as well. By way of example, Fig. 9 provides the aggregation number fraction for a BCC crystal phase and the disordered liquid for $\overline{N} = 960$ at $\chi N =$
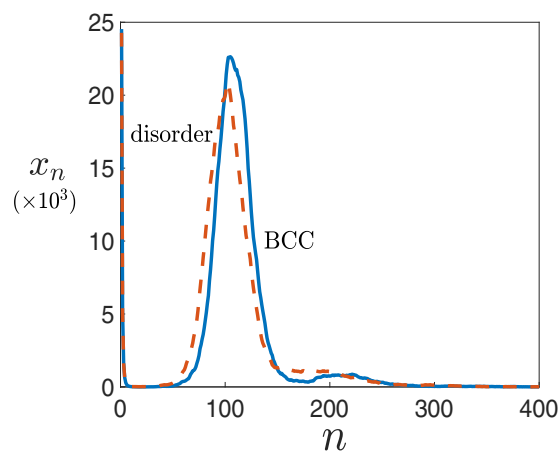

FIG. 9. Average mole fraction of chains x_n present in clusters of aggregation number n for $\overline{N} = 960$ at $\chi N = 68.5$ for the BCC phase (solid line) and the disordered phase (dashed line).
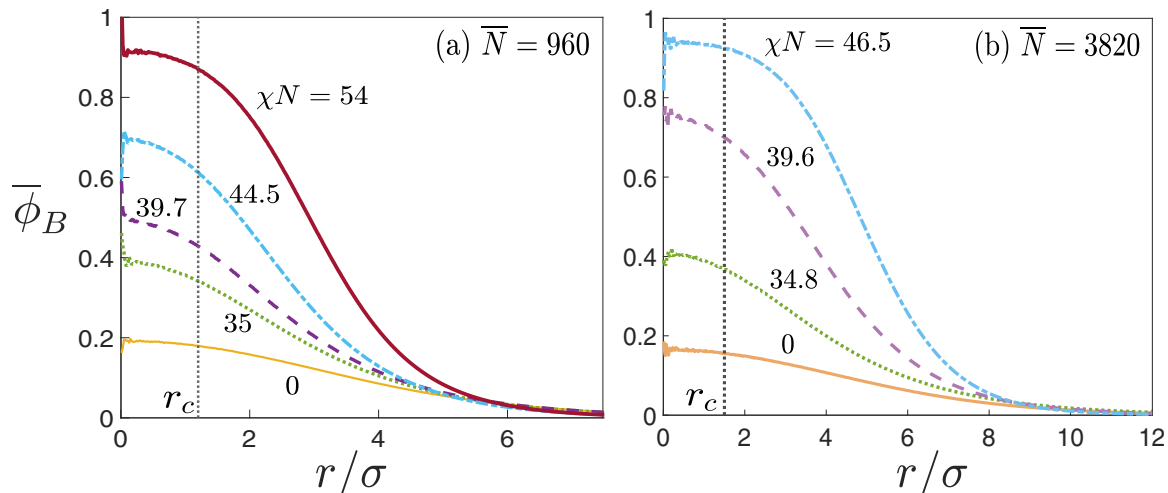
FIG. 10. Local volume fraction of the minority B-block as a function of the distance from the micelle center for different values of χN for (a) $\overline{N} = 960$ and (b) $\overline{N} = 3820$. The dotted vertical lines indicate the distances r_c used to compute the core volume fractions $\phi_B^{(c)}$. Note that the abscissa scales are different in the two panels. Panel (b) reproduced with permission from Ref. [8].

68.5. Interestingly, the cluster analysis clearly shows that micelles exhibit a polydispersity in the ordered phase as well as in the disordered phase: Note that the width of the primary peak in x_n in Fig. 9 is rather similar for both the ordered and disordered systems. Relative frequencies of micelles of different aggregation numbers can be related to corresponding differences in free energies of a hypothetical system containing one test micelle of constrained aggregation number in a fluctuating environment. The observation of similar polydispersities in crystal and liquid phases thus can be rationalized if we assume that the free energy differences associated with changes in aggregation number are controlled primarily by changes in intramicellar free energy contributions rather than free energies arising from changes in the surrounding liquid or crystal of neighboring micelles that must be made to accommodate a change in the aggregation number of a test micelle. We expect these intramicellar contributions, which arise primarily from changes in chain stretching and changes in the area of AB interface surrounding the core block of the test micelle, to be very similar in liquid and crystal phases.

Returning our attention to the distributions for x_n in the disordered system in Fig. 6, we note that the data for $\overline{N} = 3820$ and $\chi N = 46.5$ exhibits a small second maximum at a value of n approximately twice that at which x_n exhibits a primary maximum. An analogous secondary feature is even more clearly visible in the cluster distribution for a BCC crystal shown in Fig. 9. We discuss the physical origin of this feature in the penultimate section of this paper, where we show that it arises from the formation of a small population of dimers consisting of two spherical micelles with connected cores regions.

V. MICELLE STRUCTURE

We focus in this section on analyzing the spatial structure of clusters with aggregation numbers within a range that corresponds to the main peak in the distribution for x_n, which we refer to here as micellar clusters. In well-segregated systems, for which the probability density for x_n exhibits a local mini-

mum and a local maximum, we consider clusters for which n lies between the value at the local minimum and 1.6 times the value at the local maximum, as in our calculations of $Z(q)$ and x_{free}. At lower values of χN, for which x_n decreases monotonically with n, we consider clusters with n in a range 20–140 for $\overline{N} = 960$ and 30–160 for $\overline{N} = 3820$. We then characterize the concentration profile of a micelle by considering how the average composition of the resulting population of clusters varies with distance from the center of mass (COM) of the the B (minority block) beads in each such cluster. We define the effective volume fraction ϕ_B of B beads within a region of volume ΔV as the ratio $\phi_B \equiv m_B/c\Delta V$, where m_B is the actual number of B beads in the region, and c is the monomer concentration (see Table I).

Let $\overline{\phi}_B(r)$ denote the average volume fraction of B beads at a distance r from the COM of a cluster. We compute this quantity from the average of ϕ_B over a thin spherical annular region of inner radius r around the COM of each cluster, averaged over time and over all micellar clusters that satisfy the above constraints on n [8]. Figure 10 shows the results of the calculation of $\overline{\phi}_B(r)$ in the disordered phase. In the analysis for $\overline{N} = 3820$, which we reported previously [8], the observed value of $\overline{\phi}_B(r = 0)$ at the micelle COM is found to be nonzero for all values of χN, but to increase particularly rapidly over a narrow range of values of χN centered around $(\chi N)_{\text{odt}}^{\text{scf}} = 36.6$, and to saturate to values that approach unity at higher values of χN. Analogous behavior is seen here for $\overline{N} = 960$, but the increase in $\overline{\phi}_B(r = 0)$ is somewhat more gradual and occurs at somewhat higher values of χN.

At sufficiently low values of χN, for which x_n is a monotonically decreasing function, the clusters that are identified by our algorithm are not true micelles, but more diffuse geometrical clusters that arise from random contacts between minority block beads. Our measurement of $\overline{\phi}_B(r)$ at values of χN comparable to $(\chi N)_{\text{odt}}^{\text{scf}}$ presumably includes contributions both from such diffuse clusters and from micelles with a more dense core region. To distinguish these two sub-populations, we have considered the probability distribution for the effective volume fraction ϕ_B within a small spherical region at the
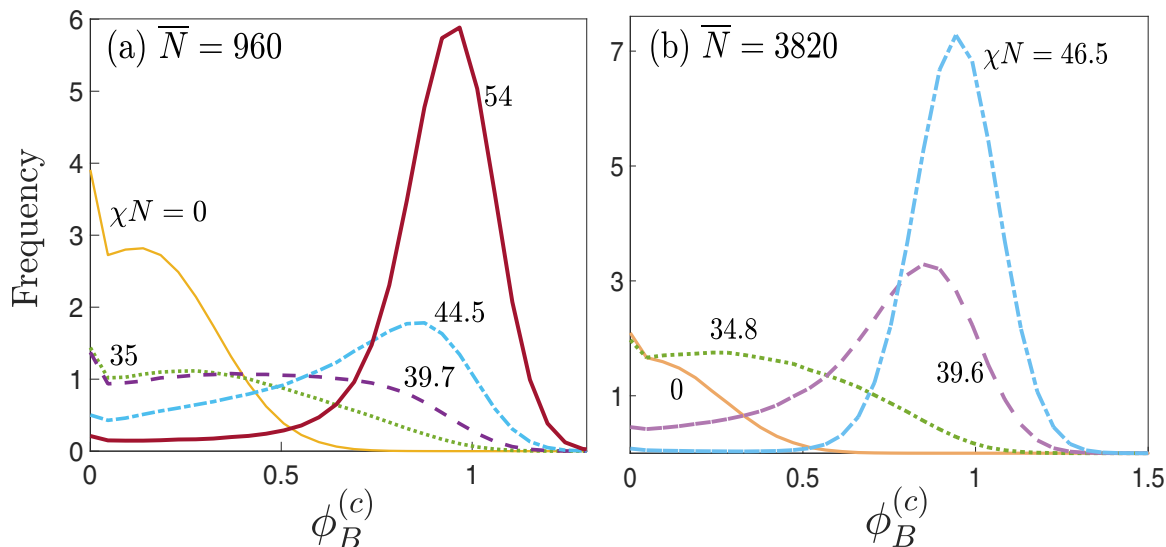
FIG. 11. Probability density for the minority block volume fraction in the micelle core at different values of χN for (a) $\overline{N} = 960$ and (b) $\overline{N} = 3820$. Note that the axis limits differ between the two panels. Panel (b) reproduced with permission from Ref. [8].

center of each cluster. We define $\phi_B^{(c)}$ to be the value of ϕ_B within a sphere of radius r_c of the cluster COM of mass, and use cutoff radii $r_c = 1.5\sigma$ for $\overline{N} = 3820$ and $r_c = 1.2\sigma$ for $\overline{N} = 960$; the values are indicated in Fig. 10 as vertical dotted lines. These values of r_c were chosen so as to be small enough to remain within the B-rich core region of a well segregated micelle, but large enough to contain many beads. Denoting ΔV as the volume of the core region, these choices for r_c furnish $c\Delta V = 21.7$ for $\overline{N} = 960$ and $c\Delta V = 21.2$ for $\overline{N} = 3820$ using the monomer concentrations c in Table I.

Figure 11 shows the calculated probability distributions of $\phi_B^{(c)}$. For $\overline{N} = 960$, the most probable volume fraction is $\phi_B^{(c)} = 0$ for $\chi N = 0$ and 35, characteristic of diffuse clusters. At $\chi N = 39.7$, we obtain a broad distribution of values of $\phi_B^{(c)}$, suggesting the coexistence of both diffuse and dense clusters at this value. At $\chi N \geqslant 44.5$, we see clear evidence of a peak with a maximum at $\phi_B^{(c)} \simeq 1$, indicating the emergence of a new population of proper micelles with a core region that is nearly pure B. As shown in Fig. 11(b), results for $\overline{N} = 3820$, which we reported previously [8], show the emergence of proper micelles at somewhat lower values of χN closer to $(\chi N)_{\text{odt}}^{\text{scf}}$.

To identify the emergence of micelles, Fig. 12 shows results for the most probable value of $\phi_B^{(c)}$ and its mean value as a function of χN. The results for $\overline{N} = 3820$ have been reported previously [8]. The most probable value shows a discontinuous jump with increasing χN from a most probable value of $\phi_B^{(c)} = 0$ at lower values of χN to a nonzero value comparable to unity at higher values. The value of χN at which the most probable value of $\phi_B^{(c)}$ becomes nonzero provides a simple estimate of the value of χN at the CMT [8]. The jump in the most probable value occurs very near $(\chi N)_{\text{odt}}^{\text{scf}} = 36.6$ for $\overline{N} = 3820$, but occurs at a slightly higher value of $\chi N \simeq 40 - 45$ for $\overline{N} = 960$. The mean value of $\phi_B^{(c)}$, shown in Fig. 12(b), shows a somewhat more smeared sigmoidal behavior centered around a higher value of χN for $\overline{N} = 960$ than for $\overline{N} = 3820$.

VI. MICELLE DIMERS

We now consider the interpretation of the secondary feature visible in Figs. 6 and 9, in which some plots of x_n show a secondary maximum at an aggregation number approximately twice that of value at which x_n is maximum. Figure 13 replots the data for x_n on a semilogarithmic scale, so as to emphasize this secondary feature. In each plot, results for both ordered and disordered phases are shown at the lowest value of χN for which an initially ordered structure was found to remain stable ($\chi N = 68.5$ for $\overline{N} = 960$ and $\chi N = 46.5$ for $\overline{N} = 3820$). Results for ordered phases for both values of $\overline{N}$ (dashed red lines) show the existence of multiple local maxima at values of n that are approximately equal to integer multiples of the value of n at first local maximum. Results obtained in the disordered phase (solid blue lines) differ with $\overline{N}$. Data for the higher $\overline{N} = 3820$ show a clear second local maximum at $n \simeq 2n^*$, whereas there is a shoulder for $\overline{N} = 960$. We show in what follows that clusters with $n \simeq 2n^*$ correspond primarily to pairs of spherical micelles with core blocks connected by threads or bridges of minority block material, each of which our cluster analysis algorithm identifies as a single larger cluster. Similarly, the higher order bumps in plots of x_n in the ordered phase correspond to groups of three or more micelles with core regions that are connected in a way that causes our algorithm to identify each as a single cluster. The frequent formation of dimers in both the disordered and ordered states of a neat diblock copolymer may provide an additional mechanism for chain exchange that could be relevant to the interpretation of observed differences in exchange rates in micellar systems with different concentration [41].

Further information about micelle structure can be obtained by characterizing each micelle by a measure of shape anisotropy [42] as well as aggregation number. Let **S** denote a cluster gyration tensor, defined as a matrix with elements

$$S_{\alpha\beta} = \frac{1}{N} \sum_{i=1}^{N} r_{i\alpha} r_{i\beta} \quad , \tag{4}$$
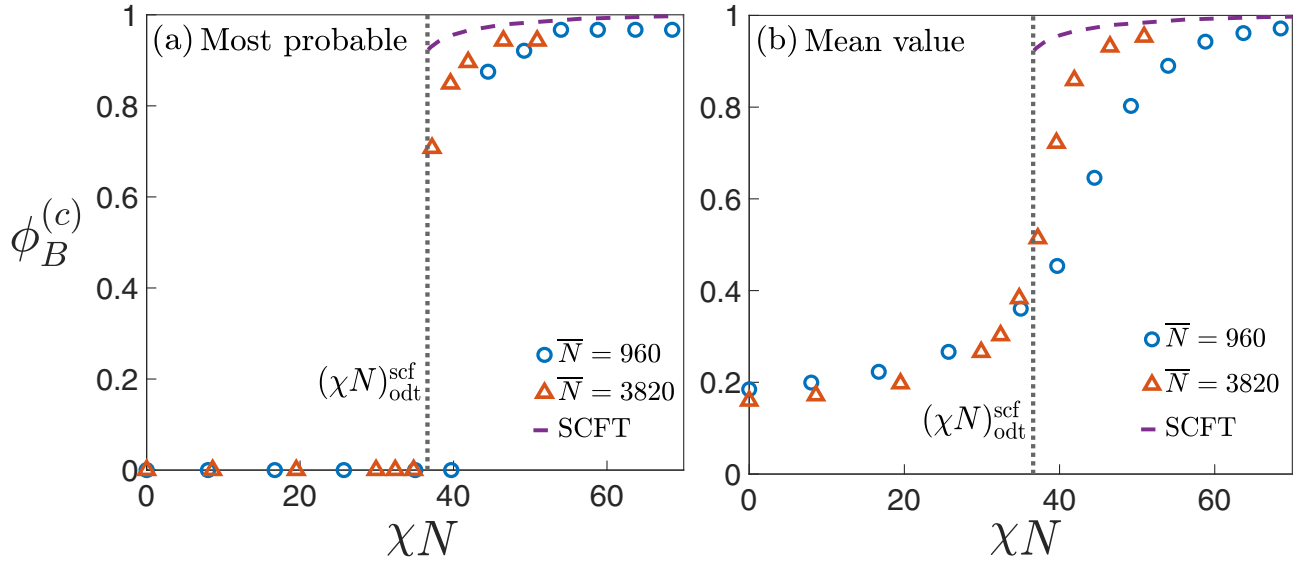
FIG. 12. Statistical characteristics of the minority component core volume fraction $\phi_B^{(c)}$. (a) Most probable value of $\phi_B^{(c)}$ for both models ($\overline{N} = 960$ and $\overline{N} = 3820$). (b) Mean value of $\phi_B^{(c)}$ for both models. In both plots, the vertical-dotted line shows the SCFT ODT value $(\chi N)_{\text{odt}}^{\text{scf}}$, and the dashed purple line shows the SCFT prediction for the the average B volume fraction at the center of a micelle within a BCC crystal for $\chi N > (\chi N)_{\text{odt}}^{\text{scf}}$.

where $r_{i\alpha}$ denotes Cartesian component α of the position of the ith minority block (B) bead within a cluster, measured relative to the center-of-mass of the B beads in the cluster, and N is the number of such beads in the cluster. Let Δ denote the shape anisotropy defined as

$$\Delta = \frac{3}{2} \frac{\lambda_1^2 + \lambda_2^2 + \lambda_3^2}{(\lambda_1 + \lambda_2 + \lambda_3)^2} - \frac{1}{2} \quad , \quad (5)$$

where λ_1, λ_2, and λ_3 are the eigenvalues of the gyration tensor **S**. Note that $\Delta = 0$ for a spherically symmetric cluster, for which all three eigenvalues are equal, and $\Delta \simeq 1$ for a rod-like cluster, for which one eigenvalue is much larger than the other two.

Figure 14 furnishes a heat map of the two-dimensional (2D) joint probability of finding a cluster with a specified pair of values of n and Δ in the ordered BCC phase at (i) $\chi N = 68.5$ for $\overline{N} = 960$ and (ii) $\chi N = 46.5$ for $\overline{N} = 3820$. Note that the primary maximum in each plot, corresponding to the main peak in a corresponding plot of x_n versus n, is located at a small value of $\Delta < 0.1$, indicating that the peak around this maximum corresponds to a set of nearly spherical micelles. The secondary maximum in each plot appears at a value of n approximately twice that of the primary peak but now with a rather large shape anisotropy of $\Delta \simeq 0.7$. This secondary maximum, which corresponds to the second peak in x_n versus n, thus arises from a population of much more anisotropic objects.
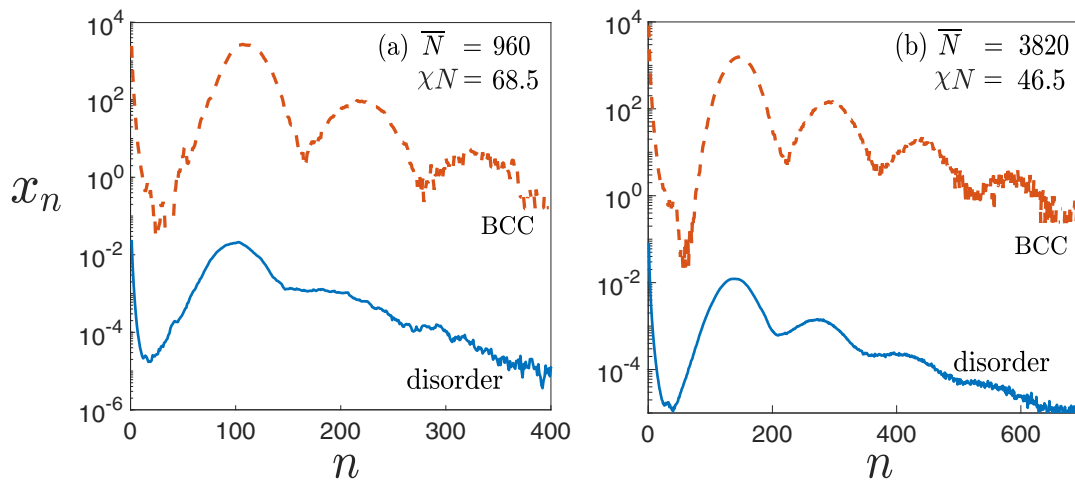

FIG. 13. Semilogarithmic plot of the mole fraction x_n of aggregation number n for the disordered phase (solid-blue line) and ordered BCC phase (dashed-red line). Results for the BCC phase are vertically shifted for clarity by multiplying x_n by 10^6. Data for (a) $\overline{N} = 960$ are for $\chi N = 68.5$ and (b) data for $\overline{N} = 3820$ are at $\chi N = 46.5$. Note that the axis limits differ between panels.
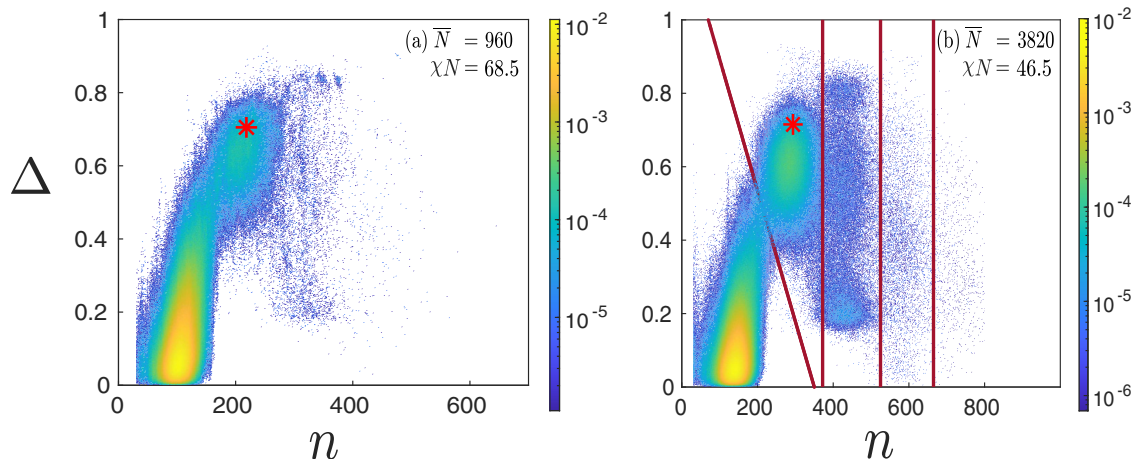
FIG. 14. Heat map for the joint probability density of specified aggregation number n and shape anisotropy Δ in simulations of the BCC ordered phase for (a) $\overline{N} = 960$ at $\chi N = 68.5$ and (b) $\overline{N} = 3820$ at $\chi N = 46.5$. The red star marker in each plot is the theoretically calculated shape anisotropy for a dimer of two micelles on nearest-neighbor lattice positions. Straight lines in (b) are boundaries of the regions used to divide clusters into individual micelle and micelle multiplets of different multiplicity. Note that the abscissa scales differ between panels.

We now show that the secondary peak in these 2D plots arises from micelle dimers. The red star markers in both plots of Fig. 14 show the predicted values of Δ for an idealized model of a dimer consisting of two nearest-neighbor micelles within a BCC lattice. The model used to compute this value consists of two spherical micelle cores with $\phi_B = 1$ within a region of radius R, separated by a distance X between the sphere centers. This model can be shown to yield

$$\Delta = \frac{3}{2} \frac{[0.4 + 2(X/2R)^2]^2 + 0.32}{[1.2 + 2(X/2R)^2]^2} - \frac{1}{2} \quad . \quad (6)$$

To obtain the values shown in Fig. 14, the intermicelle distance X has been set equal to the distance between nearest neighbors in a perfect BCC lattice in the simulated unit cell, while the core radius R has been chosen so that the number $(4\pi R^3/3)c$ of monomers in each micelle core in the model corresponds to the number of B monomers in a micelle of aggregation number equal to the most probable aggregation number. The prediction of this idealized model is seen to be

very close to the observed value of Δ at the secondary local maximum in the 2D histogram, confirming that this maximum corresponds to a population of nearest neighbor micelle dimers within a micelle crystal.

Red lines in Fig. 14(b) show boundaries that we have constructed to divide the population of all clusters within a simulation of an ordered BCC crystal into regions corresponding to nearly spherical micelle "unimers" (corresponding to the main peak in x_n versus n), micelle dimers, trimers, and (rare) quadrimers. Dimers are aligned along {111} directions, producing a single peak in the heat map. There are three types of trimers in which the two end unimers are at the corners of a cube and aligned along a {100}, {110}, or {111} direction relative to each other, producing the lobes in the trimer distribution.

To test the consistency of this classification scheme, we count the total number of micelles in the system, denoted by K, by counting each cluster in the unimer region of the 2D histogram as a single micelle, each cluster in the dimer region
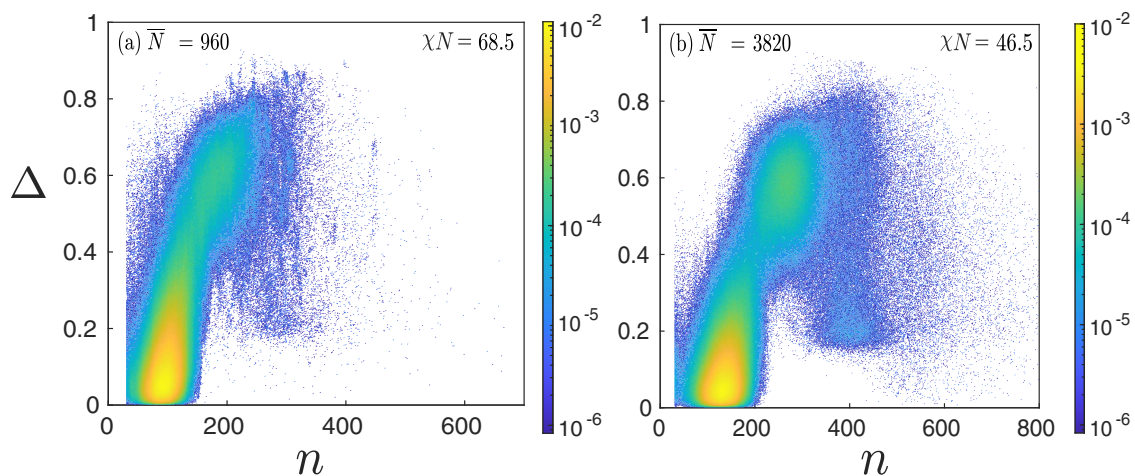

FIG. 15. Heat map for the frequency of observing shape anisotropy Δ and aggregation number n, similar to Fig. 14, but now for the disordered phase for (a) $\overline{N} = 960$ at $\chi N = 68.5$ and (b) $\overline{N} = 3820$ at $\chi N = 46.5$. Note that the abscissa scales differ between panels.
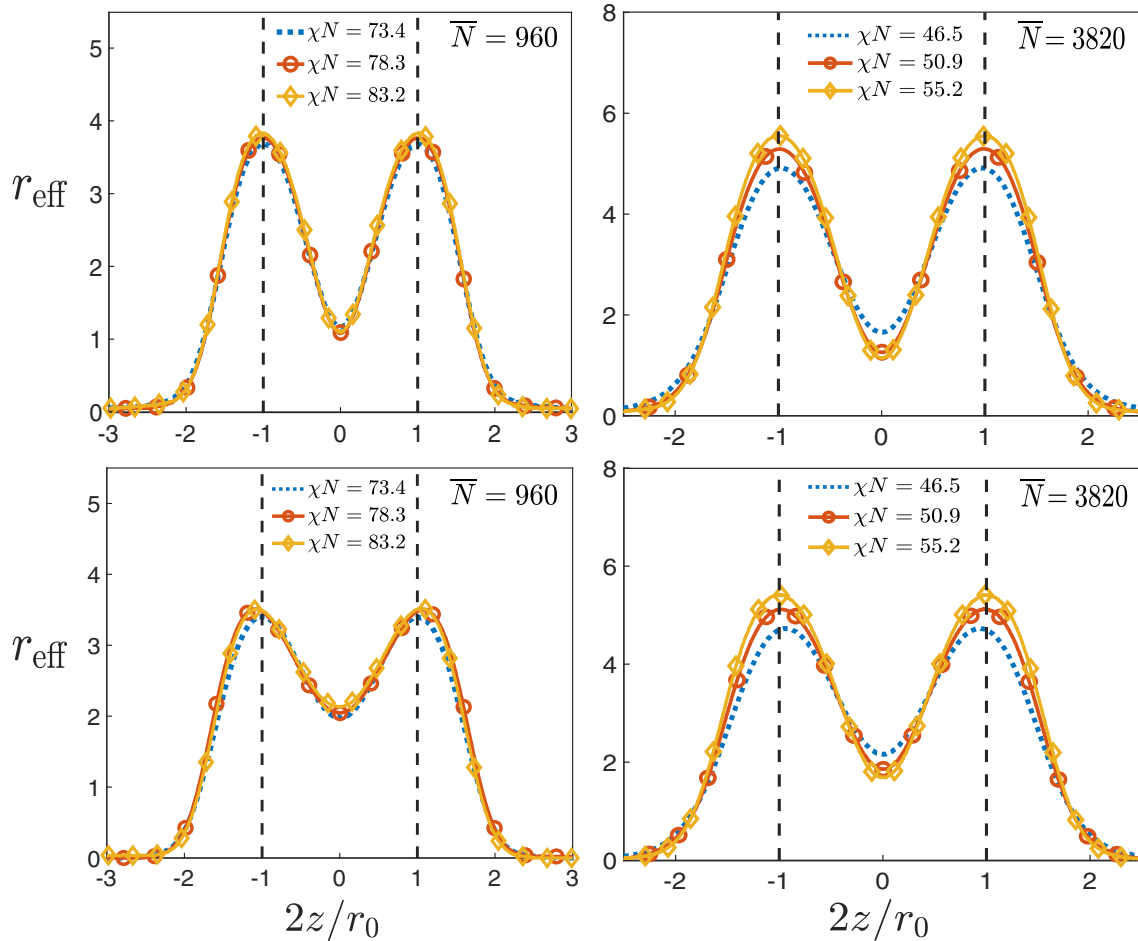
FIG. 16. Short lived (top row) and long lived (bottom row) micelle dimer profiles showing the variation in an effective radius r_{eff} vs the distance z from the center of the micelle dimer. z is normalized by $r_0/2$ where r_0 is the distance between the nearest-neighboring micelles in a BCC crystal with a unit cell length of $L/3$ where L is the simulation box length. r_{eff} is given in simulation units, in which the range σ of the pair interaction is set to unity. Note that the axis limits differ between panels.

as two micelles, and so on for trimers and quadrimers. In a simulated system designed to accommodate a BCC lattice of 54 micelles, for $\overline{N} = 960$ and $\chi N = 78.3$, this scheme yields a mean value of K of 54.00 with a very small standard deviation of 0.003 micelles, thereby confirming that the scheme correctly categorizes almost all clusters within such a crystal as either individual micelles or micelle multiplets. A similar classification was developed for all simulations of ordered phases for both models, and verified using the same methodology.

Using this classification scheme, we can unambiguously count the number of bridges between nearest-neighbor micelles within a BCC crystal, and the fraction of all possible nearest-neighbor "bonds" within a BCC crystal along which there are such bridges between micelles. This fraction was less than 0.02 (i.e., less than 2%) for all the cases considered here, and decreases with increasing χN.

We have performed a similar analysis for the disordered state in Fig. 15, using the same values of χN as in Fig. 14. The structure in the disordered phase is qualitatively similar to that in the ordered phase. In the disordered phase, however, the main and secondary peaks are less well separated, suggesting

a somewhat greater tendency for micelles to form elongated objects of intermediate aggregation number in addition to simple micelle "dimers".

We next consider the geometrical structure of a population of clusters formed from micelle dimers. For this purpose, it is useful to use the eigenvectors of the gyration tensor $\mathbf{S}$ to define a coordinate system for each cluster. In an idealized model of the minority beads of a dimer as a dumbbell consisting of two connected spheres, the eigenvector of $\mathbf{S}$ associated with its largest eigenvector would lie along the axis connecting the centers of the spheres. To characterize real clusters, we thus define a coordinate z for each B bead given by the distance projection of its position relative to the cluster center-of-mass onto the eigenvector of $\mathbf{S}$ associated with the largest eigenvalue. Given a population of clusters generated by a simulation, we then can compute a histogram of values of z for all B monomers belonging to molecules in each cluster, and use this histogram to create a one dimensional density $\rho(z)$ at each value of z, defined such that $\int dz \rho(z)$ is the average number of B monomers per cluster. We then define an effective radius $r_{\text{eff}}(z)$ at each value of z to be the radius of a hypothetical cylindrically symmetric object of monomer concentration c

that would give the same one-dimensional density $\rho(z)$ as that measured in the simulation, such that $\rho(z) = c\pi r_{\mathrm{eff}}^2$, where c is the average total monomer concentration in the simulation model (Table I).

In our analysis of $r_{\mathrm{eff}}(z)$, it proves important to take into account that micelle dimers and other multiplets are transient structures that are constantly formed when new bridges are created between nearby micelles and destroyed when bridges break. An analysis of the dynamics of these processes is given in the SM [37]. We find that a significant fraction of dimers are very short-lived structures that break apart in less than 1000 molecular dynamics time steps. There is, however, also a smaller fraction that is stable for thousands of time steps. In our analysis of structure, we present separate results for short lived and long-lived dimers within a BCC crystal. For this purpose, we classify a dimer as long-lived if it survived for at least 1000 timesteps, and short-lived if it survived for less than 1000 steps.

The values of the effective radius r_{eff} as a function of position z along the main axis of the dimers within a BCC crystal appears in Fig. 16. Results are plotted as functions of a normalized coordinate $2z/r_0$ in which r_0 is the distance between nearest-neighbor lattice points in a perfect $3 \times 3 \times 3$ BCC crystal constructed within the simulation unit cell. In a simplified model of a dimer as two connected spheres, this would yield $2z/r_0 = \pm 1$ at the centers of the spheres. The value of r_{eff} at the local maxima that occur at approximately these values thus correspond approximately to the radii of the micelle cores. The fact that $r_{\mathrm{eff}}(z)$ exhibits local maxima very close to $2z/r_0 = \pm 1$ indicates that connected micelles within a BCC crystal remain very close to their ideal lattice positions. Each plot of $r_{\mathrm{eff}}(z)$ versus z also shows a local minimum at $z = 0$. The value at this local minimum is a measure of the radius of the bridge of B monomers that connects the two micelle cores. The fact that all of these plots show a distinct minimum confirms that these are clusters do indeed all have a dimer or "dumbbell" shape with mass concentrated near the two ends, rather than a more uniform rod-like distribution. The ratio of the the bridge radius to micelle core radius ranges from 0.2 to 0.3 for short-lived dimers and 0.4 to 0.55 for the long-lived dimers. The bridges between micelles appear to be thick enough to be visualized as bridges formed by the core blocks of multiple molecules, rather than more tenuous single-molecule bridges, particularly for the long-lived dimers.

VII. SUMMARY

The present contribution builds substantially on our preliminary communication on simulations of disordered asymmetric diblock copolymer melts [8], which focused solely on a limited analysis of the results obtained at the higher invariant degree of polymerization $\overline{N} = 3820$ available from Model S2-64. Here, we have investigated those same properties at an even more experimentally-relevant value of $\overline{N} = 960$ using Model S1-64, and we have provided additional information on the structure, dynamics, and thermodynamics for both values of $\overline{N}$. In this final section, we summarize the key outcomes of our analysis of the simulation data and their implications for experiments and theory.

Overall, the results presented here support the picture of the disordered micelle state described in our prior paper [8]. Explicitly, we found previously [8] for $\overline{N} = 3820$ that there exists (i) a shoulder in $S(q)$ as χN increases in the disordered state that is not predicted by the RPA (Fig. 2); (ii) a systematic deviation from the linear dependence of $S^{-1}(q)$ that is roughly coincident with the ODT predicted by SCFT but without the sudden decrease of $S^{-1}(q)$ that would accompany an order-disorder transition (Fig. 3); and (iii) a clear emergence of a population of a peak in the average mole fraction of chains with aggregation number n above the SCFT ODT (Fig. 6) where the nearly spherical micelles have cores that are almost pure (Figs. 11 and 12). Taken together, these data support a model where the CMT is roughly coincident with the ODT predicted by SCFT [8], with the true ODT taking place at a higher value of χN.

Inspection of Figs. 2, 3, 6, 11, and 12 shows that the picture we developed previously [8] at $\overline{N} = 3820$ holds for the substantially lower value of $\overline{N} = 960$ investigated here, albeit with smaller aggregation numbers and larger values of χN at $\overline{N} = 960$ required to produce the phenomena seen at $\overline{N} = 3820$. The most notable effects of $\overline{N}$ are qualitative differences in the structure factor near the SCFT ODT. Namely, results for the system with a larger value of $\overline{N} = 3820$ exhibit a weak inflection at $\chi N \simeq (\chi N)_{\mathrm{odt}}^{\mathrm{scf}}$ in a plot of $S^{-1}(q^*)$ versus χN. The analogous plot for the system with a smaller value of $\overline{N} = 960$ does not, however, exhibit such an inflection, and instead exhibits behavior qualitatively similar to that observed in studies of more nearly symmetric copolymers [26,28,40]. We assume that the inflection in this plot would become sharper for systems of even greater $\overline{N}$, approaching a discontinuous jump in the limit $\overline{N} \to \infty$, but that it is washed out in systems of modest $\overline{N}$ for which both the appearance of micelles and the build-up of correlations in micelle position is found to occur over a wider range of values of χN. The appearance of an inflection in a plot of $S^{-1}(q^*)$ versus χN (or, equivalently, inverse temperature $1/T$) thus seems to provide a reliable signature of the CMT only in systems with very large values of $\overline{N}$. Overall, our results confirm the existence of a crossover from molecularly disordered regime to a liquid of micelles with increasing χN, and suggest that, with increasing $\overline{N}$, the crossover occurs over an increasingly narrow range of values of χN centered around a value that rapidly approaches $(\chi N)_{\mathrm{odt}}^{\mathrm{scf}}$, in qualitative agreement with earlier theoretical predictions [33,34].

In addition to the approaches used in our prior paper [8] to identify the onset of the disordered micellar liquid, we have developed new evidence here by analyzing the structure factor in the context of the Percus-Yevick theory [20] in Fig. 5, which has impact on analyses of scattering data in experiments. The peaks in the intermicellar correlations $Z(q)$ occur at the same wavenumbers q of the corresponding features in the structure factor $S(q)$. This correspondence between features in $Z(q)$ and $S(q)$ is largely independent of $\overline{N}$. Our analysis of $Z(q)$ shows, however, that micelles are present at significantly lower values of χN than those at which this feature becomes visible, because correlations in micelle positions remain rather weak near the CMT. Analysis of both $S(q)$ and $Z(q)$ also clearly shows that the strength of correlations among micelle positions increases more rapidly

with increasing χN in systems of greater $\overline{N}$. Observation of this secondary feature in $S(q)$ thus indicates the existence of a correlated liquid of micelles, but is not a sufficiently sensitive indicator to be used to identify the CMT.

Our analysis of the primary peak in the structure factor (Fig. 4), the derivative of the free energy with χN (see SM [37]), the fraction of free chains (Fig. 7), and the most probable micelle aggregation number (Fig. 8) show that predictions from SCFT for ordered BCC structures provides remarkably good estimates for these properties in the disordered micellar liquid. These results support prior work [29,30,32] comparing SCFT predictions to simulations of disordered diblock copolymer melts. Unfortunately, we were unable to determine definitively how much the true ODT in our simulations deviates from the SCFT prediction; initially ordered systems spontaneously melt at sufficiently low χN, but initially ordered systems fail to crystallize in our simulations. The lower bounds on $(\chi N)_{\mathrm{odt}}$ obtained here (see SM [37]) are, however, enough to show that the difference $(\chi N)_{\mathrm{odt}} - (\chi N)_{\mathrm{odt}}^{\mathrm{scf}}$ between values of χN at the actual and SCFT predictions for the order-disorder transition is substantially greater than the difference between the value at the CMT and the predicted SCFT transition. If we tentatively treat these lower bounds as the best available estimates of $(\chi N)_{\mathrm{odt}}$, the results suggest that $(\chi N)_{\mathrm{odt}}$ increases rather rapidly with decreasing $\overline{N}$ in the experimentally relevant range of values.

The cluster analysis presented here shows the existence of a small but easily measurable population of micelle dimers at conditions near the order-disorder transition. Evidence of dimers was found in both ordered and disordered phases, but the analysis and evidence are particularly clear in the ordered phase. Analysis of dynamics in the ordered phase, discussed in the SM [37], showed frequent formation and rapid destruction of bridges between the core blocks of nearest-neighbor micelles. The presence of these short-lived dimers is not expected to affect most experimentally accessible properties, but drew our attention in part because we found that it complicates attempts to use our cluster analysis to characterize dynamics in these systems by identifying elementary dynamical processes such as unimer insertion and expulsion and micelle fission or fusion. We anticipate that the dynamics of the disordered micelle liquid will be a fruitful avenue for future work.

[1] D. Kinning and E. Thomas, Hard-sphere interactions between spherical domains in diblock copolymers, Macromolecules **17**, 1712 (1984).

[2] M. Schwab and B. Stühn, Thermotropic Transition from a State of Liquid Order to a Macrolattice in Asymmetric Diblock Copolymers, Phys. Rev. Lett. **76**, 924 (1996).

[3] M. Schwab and B. Stühn, Asymmetric diblock copolmers-phase behavior and kinetics of structure formation, Colloid Polym. Sci. **275**, 341 (1997).

[4] J. L. Adams, D. J. Quiram, W. M. Graessley, R. A. Register, and G. R. Marchand, Ordering dynamics of compositionally asymmetric styrene-isoprene block copolymers, Macromolecules **29**, 2929 (1996).

[5] X. Wang, E. E. Dormidontova, and T. P. Lodge, The order-disorder transition and the disordered micelle regime for poly(ethylenepropylene-b-dimethylsiloxane) spheres, Macromolecules **35**, 9687 (2002).

[6] J. K. Kim, H. H. Lee, S. Sakurai, S. Aid, J. Masomoto, S. Nomura, Y. Kitagawa, and Y. Suda, Lattice disordering domain dissolution transitions in polystyrene-block-poly(ethylene-co-but-1-ene)-block-polystyrene triblock copolymers having a highly asymmetric composition, Macromolecules **32**, 6707 (1999).

[7] C. D. Han, N. Y. Vaidya, D. Kim, G. Shin, D. Yamaguchi, and T. Hashimoto, Lattice disordering/ordering and demicellization/micellization transitions in highly asymmetric polystyrene-block-polyisoprene copolymers, Macromolecules **33**, 3767 (2000).

[8] A. Chawla, F. S. Bates, K. D. Dorfman, and D. C. Morse, Identifying a critical micelle temperature in simulations of disordered asymmetric diblock copolymers, Phys. Rev. Materials **5**, L092601 (2021).

[9] G. Ungar, Y. Liu, X. Zeng, V. Percec, and W.-D. Cho, Giant supramolecular liquid crystal lattice, Science **299**, 1208 (2003).

[10] X. Zeng, G. Ungar, Y. Liu, V. Percec, A. E. Dulcey, and J. K. Hobbs, Supramolecular dendritic liquid quasicrystals, Nature (London) **428**, 157 (2004).

[11] S. Lee, M. J. Bluemle, and F. S. Bates, Discovery of a Frank-Kasper σ phase in sphere-forming block copolymer melts, Science **330**, 349 (2010).

[12] M. Huang, C.-H. Hsu, J. Wang, S. Mei, X. Dong, Y. Li, M. Li, H. Liu, W. Zhang, T. Aida *et al.*, Selective assemblies of giant tetrahedra via precisely controlled positional interactions, Science **348**, 424 (2015).

[13] K. Yue, M. Huang, R. L. Marson, J. He, J. Huang, Z. Zhou, J. Wang, C. Liu, X. Yan, K. Wu *et al.*, Geometry induced sequence of nanoscale Frank-Kasper and quasicrystal mesophases in giant surfactants, Proc. Natl. Acad. Sci. USA **113**, 14195 (2016).

[14] K. Kim, M. W. Schulze, A. Arora, R. M. Lewis, III, A. Hillmyer, K. D. Dorfman, and F. S. Bates, Thermal processing of diblock copolymer melts mimics metallurgy, Science **356**, 520 (2017).

[15] S. A. Kim, K. J. Jeong, A. Yethiraj, M. K. Mahanthappa, J. Jeong, A. Yethiraj, and M. K. Mahanthappa, Low-symmetry sphere packings of simple surfactant micelles induced by ionic sphericity, Proc. Natl. Acad. Sci. USA **114**, 4072 (2017).

[16] C. M. Baez-Cotto and M. K. Mahanthappa, Micellar mimicry of intermetallic C14 and C15 laves phases by aqueous lyotropic self-assembly, ACS Nano **12**, 3226 (2018).

[17] Z. Su, C.-h. Hsu, Z. Gong, X. Feng, J. Huang, R. Zhang, Y. Wang, J. Mao, C. Wesdemiotis, T. Li *et al.*, Identification of a Frank-Kasper Z phase from shape amphiphile self-assembly, Nat. Chem. **11**, 899 (2019).

[18] M. W. Bates, J. Lequieu, S. M. Barbon, R. M. Lewis, III, K. T. Delaney, A. Anastasaki, C. J. Hawker, G. H. Fredrickson, and C. M. Bates, Stability of the A15 phase in diblock copolymer melts, Proc. Natl. Acad. Sci. USA **116**, 13194 (2019).

[19] K. D. Dorfman, Frank-Kasper phases in block copolymers, Macromolecules **54**, 10251 (2021).

[20] J. K. Percus and G. J. Yevick, Analysis of classical statistical mechanics by means of collective coordinates, Phys. Rev. **110**, 1 (1958).

[21] S. Lee, C. Leighton, and F. S. Bates, Sphericity and symmetry breaking in the formation of Frank–Kasper phases from one component materials, Proc. Natl. Acad. Sci. USA **111**, 17723 (2014).

[22] M. W. Matsen and M. Schick, Stable and Unstable Phases of a Diblock Copolymer Melt, Phys. Rev. Lett. **72**, 2660 (1994).

[23] G. H. Fredrickson and E. Helfand, Fluctuation effects in the theory of microphase separation in block copolymers, J. Chem. Phys. **87**, 697 (1987).

[24] P. Grzywacz, J. Qin, and D. C. Morse, Renormalization of the one-loop theory of fluctuations in polymer blends and diblock copolymer melts, Phys. Rev. E **76**, 061802 (2007).

[25] J. Qin, P. Grzywacz, and D. C. Morse, Renormalized one-loop theory of correlations in diblock copolymers, J. Chem. Phys. **135**, 084902 (2011).

[26] J. Qin and D. C. Morse, Fluctuations in Symmetric Diblock Copolymer Melts: Testing Theories Old and New, Phys. Rev. Lett. **108**, 238301 (2012).

[27] J. Glaser, J. Qin, P. Medapuram, M. Müller, and D. Morse, Test of a scaling hypothesis for the structure factor of disordered diblock copolymer melts, Soft Matter **8**, 11310 (2012).

[28] J. Glaser, J. Qin, P. Medapuram, and D. C. Morse, Collective and single-chain correlations in disordered melts of symmetric diblock copolymers: Quantitative comparison of simulations and theory, Macromolecules **47**, 851 (2014).

[29] J. Glaser, P. Medapuram, T. M. Beardsley, M. W. Matsen, and D. C. Morse, Universality of Block Copolymer Melts, Phys. Rev. Lett. **113**, 068302 (2014).

[30] P. Medapuram, J. Glaser, and D. C. Morse, Universal phenomenology of symmetric diblock copolymers near the order–disorder transition, Macromolecules **48**, 819 (2015).

[31] T. Ghasimakbari and D. C. Morse, Correlations in disordered melts of asymmetric diblock copolymers, Macromolecules **51**, 2335 (2018).

[32] T. Ghasimakbari and D. C. Morse, Order-disorder transitions and free energies in asymmetric diblock copolymers, Macromolecules **53**, 7399 (2020).

[33] J. Wang, Z.-G. Wang, and Y. Yang, Nature of disordered micelles in sphere-forming block copolymer melts, Macromolecules **38**, 1979 (2005).

[34] E. E. Dormidontova and T. P. Lodge, The order-disorder transition and the disordered micelle regime in sphere-forming block copolymer melts, Macromolecules **34**, 9143 (2001).

[35] A. Semenov, Contribution to the theory of microphase layering in block-copolymer melts, Sov. Phys. JETP **61**, 733 (1985).

[36] A. Semenov, Microphase separation in diblock-copolymer melts: Ordering of micelles, Macromolecules **22**, 2849 (1989).

[37] See Supplemental Material at http://link.aps.org/supplemental/10.1103/PhysRevMaterials.6.095602 for further details of MD simulations, analysis of the structure factor, thermodynamic analysis, micelle dimer dynamics and dimer structure and Refs. [43–49].

[38] J. A. Mysona, A. V. McCormick, and D. C. Morse, Simulation of diblock copolymer surfactants. I. Micelle free energies, Phys. Rev. E **100**, 012602 (2019).

[39] L. Leibler, Theory of microphase separation in block copolymers, Macromolecules **13**, 1602 (1980).

[40] F. Bates, J. Rosedale, and G. Fredrickson, Fluctuation effects in a symmetric diblock copolymer near the order-disorder transition, J. Chem. Phys. **92**, 6255 (1990).

[41] S. H. Choi, F. S. Bates, and T. P. Lodge, Molecular exchange in ordered diblock copolymer micelles, Macromolecules **44**, 3594 (2011).

[42] D. N. Theodorou and U. W. Suter, Shape of unperturbed linear polymers: polypropylene, Macromolecules **18**, 1206 (1985).

[43] J. A. Anderson, C. D. Lorenz, and A. Travesset, General purpose molecular dynamics simulations fully implemented on graphics processing units, J. Comput. Phys. **227**, 5342 (2008).

[44] J. Glaser, T. D. Nguyen, J. A. Anderson, P. Lui, F. Spiga, J. A. Millan, D. C. Morse, and S. C. Glotzer, Strong scaling of general-purpose molecular dynamics simulations on gpus, Comput. Phys. Commun. **192**, 97 (2015).

[45] G. J. Martyna, D. J. Tobias, and M. L. Klein, Constant pressure molecular dynamics algorithms, J. Chem. Phys. **101**, 4177 (1994).

[46] G. J. Martyna, M. E. Tuckerman, D. J. Tobias, and M. L. Klein, Explicit reversible integrators for extended systems dynamics, Mol. Phys. **87**, 1117 (1996).

[47] H. Flyvbjerg and H. Petersen, Error estimates on averages of correlated data, J. Chem. Phys. **91**, 461 (1989).

[48] T. M. Gillard, P. Medapuram, D. C. Morse, and F. S. Bates, Fluctuations, phase transitions, and latent heat in short diblock copolymers: Comparison of experiment, simulation, and theory, Macromolecules **48**, 2801 (2015).

[49] S. Lee, T. M. Gillard, and F. S. Bates, Fluctuations, order, and disorder in short diblock copolymers, AIChE J. **59**, 3502 (2013).